

# Learned Kernels for Interpretable and Efficient PPG Signal Quality Assessment and Artifact Segmentation

Sully F. Chen<sup>\*</sup>, Zhicheng Guo<sup>†</sup>, Cheng Ding<sup>‡</sup>, Xiao Hu<sup>§</sup>, Cynthia Rudin<sup>¶</sup>

## Abstract

Photoplethysmography (PPG) provides a low-cost, non-invasive method to continuously monitor various cardiovascular parameters. PPG signals are generated by wearable devices and frequently contain large artifacts caused by external factors, such as motion of the human subject. In order to ensure robust and accurate extraction of physiological parameters, corrupted areas of the signal need to be identified and handled appropriately. Previous methodology relied either on handcrafted feature detectors or signal metrics which yield sub-optimal performance, or relied on machine learning techniques such as deep neural networks (DNN) which lack interpretability and are computationally and memory intensive. In this work, we present a novel method to learn a small set of interpretable convolutional kernels that has performance similar to – and often better than – the state-of-the-art DNN approach with several orders of magnitude fewer parameters. This work allows for efficient, robust, and interpretable signal quality assessment and artifact segmentation on low-power devices.

<sup>\*</sup>Duke University School of Medicine, Durham, NC 27710, USA (e-mail: sully.chen@duke.edu)

<sup>†</sup>Department of Electrical and Computer Engineering, Duke University, Durham, NC 27710, USA (e-mail: zhicheng.guo@duke.edu)

<sup>‡</sup>Department of Biomedical Engineering, Georgia Institute of Technology & Emory University Atlanta, GA 30322, USA (e-mail: chengding@gatech.edu)

<sup>§</sup>Nell Hodgson Woodruff School of Nursing Emory University, 1520 Clifton Rd, Atlanta, GA 30322, USA (e-mail: xiao.hu@emory.edu)

<sup>¶</sup>Department of Computer Science and Department of Electrical and Computer Engineering, Duke University, Durham, NC 27710, USA (e-mail: cynthia@cs.duke.edu)

## 1 Introduction

Photoplethysmography (PPG) is a non-invasive optical technique to measure blood volume changes in tissue by measuring changes in light absorption. It is commonly used to infer various cardiovascular parameters, such as blood oxygenation, heart rate, heart rate variability, and other related parameters [1–7]. It has become abundant in wearable consumer devices (i.e., smart watches) and there is a continuing effort to develop algorithms that extract meaningful data from PPG signals obtained from these devices.

A notable limitation of wearable PPG devices is their sensitivity to motion-induced artifacts, which leads to corruption in the collected signals. This challenge is further exacerbated by the ambulatory nature of most users, and the PPG signals are collected during daily activities involving movement. Motion artifacts often harm measurement quality and it requires considerable effort to either identify and discard noisy data or reconstruct these corrupted segments. Specifically, the identification of motion-induced artifacts in PPG signals is surprisingly non-trivial. Previous methods relied on either additional sensors (e.g., accelerometers) [8], statistical methods such as standard deviation, skew, kurtosis, wavelet-based motion artifact reduction algorithms [9, 10] or more sophisticated handcrafted feature detectors [11, 12], machine-learning techniques such as frequency-domain feature extraction and an ensemble of decision trees [13], or, more recently, computationally expensive deep neural networks [14, 15]. The aforementioned hand-crafted feature detectors and statistical methods provide clear indications and reasoning for why a segment is identified as an artifact,

but often underperform compared to other methods, such as deep neural networks [16–18]. However, deep neural nets contain millions of parameters, which require a significant amount of memory and computational resources, thus, making them incompatible with small, low-power wearable devices. Furthermore, deep neural networks lack interpretability; it is difficult, if not impossible, to determine a rationale behind the identification of an artifact in the PPG signal. For the same reason, they are difficult to troubleshoot.

In this work, we merge the best of all worlds: performance, interpretability, and computational efficiency. Specifically, we obtain **state-of-the-art (SotA) results in artifact segmentation**, and we have **interpretability**, all in a model with **several orders of magnitude fewer parameters** than the current SotA. We accomplish this by learning a set of convolution kernels that, when applied to the PPG signal and summed following a floor function, directly produces a measure of PPG signal quality. This measure can then be thresholded to segment and identify artifacts. Notably, this approach differs from deep convolutional neural networks in that there are no “layers” – only a single set of convolutions is applied to the signal. Furthermore, the mixing is “nearly linear,” in the sense that the only non-linearity is a floor function setting negative values to zero. Thus, we can directly and precisely measure the contribution of any individual convolution to the predicted signal quality, and positive contributions are directly proportional to the output signal. Furthermore, our approach is similar to feature-detection-based approaches in that we learn a set of kernels that mimic handcrafted features. In our approach, for our smallest model, we learn so few kernels (12 total) that we can inspect these features by eye and observe the waveforms learned by our approach with a quick glance. This contrasts with deep neural networks, where there are so many parameters one cannot feasibly inspect the inner workings of the model, and even if one took the time to organize these features, it would still be unclear how each feature individually contributes to the output due to the built-in non-linearity. Additionally, our model outputs a real-valued signal that can be interpreted as a likelihood that the signal is

an artifact, yielding a continuous value of signal quality. In our work, we threshold this value to segment artifacts, but one could conceivably use this signal to segment PPG signals into gradations of quality.

## 2 Related Work

### 2.1 Utilization of Extra Sensors

Some approaches for motion artifact detection in PPG signals involve using additional sensors to provide supplementary information about the wearer’s activity or motion. Several studies use accelerometers to detect artifacts [19–21], or even a second PPG sensor [22]. By analyzing the data from these sensors, it is possible to identify periods of high motion and correlate them with artifacts in the PPG signal. The fusion of data from multiple sensors can improve the performance of artifact detection algorithms by providing a more complete picture of the wearer’s activity. Although this approach can improve the performance of motion artifact detection, it also increases the complexity of the system and may require additional power and processing resources. Furthermore, these studies primarily focus on motion artifacts and cannot detect other sources of noise, such as noise introduced by external light sources, signal interference, or when sensors have poor skin contact.

### 2.2 Statistical Techniques

Statistical and machine learning techniques involve applying various algorithms to extract features and build classifiers for detecting motion artifacts in PPG signals. Several studies have used least-squares-based methods, such as X-LMS [23] or adaptive filters [24, 25]. Other methods have used statistical parameters like kurtosis or Shannon entropy to detect artifacts [26]. Additionally, machine learning techniques, such as support-vector machines, random forests, and naïve Bayes have also been employed [27, 28]. These methods are desirable as they are simple, explainable, and low-compute. However, they often underperform compared to deep learning-based approaches

and typically focus on classification of discrete time-chunks rather than segmentation.

### 2.3 Deep Learning Approaches

Deep learning approaches have gained popularity in recent years due to their ability to automatically learn features and patterns from large datasets. Methods such as 1D convolutional neural networks [29], 2D convolutional neural networks [30], and U-Net type architectures [31] have been implemented with excellent results. These methods can achieve high performance but at the cost of increased computational complexity and lack of interpretability. Furthermore, many of these architectures, such as 1D and 2D convolutional neural networks are not inherently designed for segmentation tasks, and must be adapted to segmentation tasks via methods like GradCAM [32] or SHAP [33], which adds another layer of complexity, and these methods are not always reliable. An excellent review of artifact-removal techniques has been provided by Pollreisz & TaheriNejad for further reference [34].

## 3 Datasets

We evaluate our approach against the same datasets used by the current state-of-the-art algorithms [31], namely PPG-DaLiA [35], WESAD [36], and TROIKA [37]. PPG-DaLiA is a multimodal dataset composed of recordings from 15 subjects performing real-world tasks. The data include electrocardiogram (ECG), accelerometer, and electrodermal recordings for various settings/activities, such as sitting still, walking up/down stairs, playing sports (soccer, cycling, walking), and driving. The WESAD data was recorded from wrist and chest PPGs from 15 subjects aged 21-55 (median 28) primarily focusing on varying the emotional state of the subject (neutral, stressed, amused). ECG, accelerometer, electrodermal, and wrist PPG signals were recorded. Lastly, the TROIKA data was recorded from subjects running on a treadmill (ages 18-35). Accelerometer, ECG, and PPG signals were recorded. This dataset represents the most challenging dataset for general-

ization since the subjects were under intense physical demands with poor signal quality owing to the large amounts of movement.

We follow the same preprocessing procedure as Guo et al. [31], namely applying a bandpass filter with cutoffs of 0.9 Hz and 5 Hz, splitting the data into 30-second chunks, and resampling to 64 Hz. However, instead of normalizing the chunks between [0, 1] as Guo et al. did, we instead opt to normalize each chunk to a unit normal distribution. We used Guo et al.’s publicly available artifact segmentation labels, which were created via a web-annotation tool and a group of skilled annotators [31].

## 4 Methods

### 4.1 Overview

In this study, we framed the task of PPG quality classification as a feature-detection task. We believed that clean PPG signals could be identified by certain common features, and PPG signals with artifacts could be identified by either the lack of these recurring features or by features shared by artifacts caused by factors such as movement. Our PPG signals are one-dimensional time-series signals, and we learned a set of kernels to identify these features.

To achieve this, we learn a set of  $M$  convolution kernels of varying numbers to evaluate parameter scaling laws:  $M = 12$  (small), 72 (medium), 384 (large). The  $M$  kernels are divided into sets of  $M/3$  kernels of short (1.0 seconds), moderate (1.5 seconds), and long (3.0 seconds) sizes, with the goal of learning features of different lengths to improve classification quality. The kernels are convolved with the input PPG signal and the values are floored via  $\max(0, x)$  to obtain a non-negative signal quality indicator. Additionally, a bias is added to each convolution channel. We compute a weighted sum of the convolutions to produce a single channel that represents a measure of signal quality, which is then transformed to range [0.0, 1.0] via the sigmoid function. We apply a 3rd-order Savitzky-Golay filter ( $\sim 0.8$ -second filter window) to smooth the output, then apply thresholding at a value of 0.5 to produce a binary output

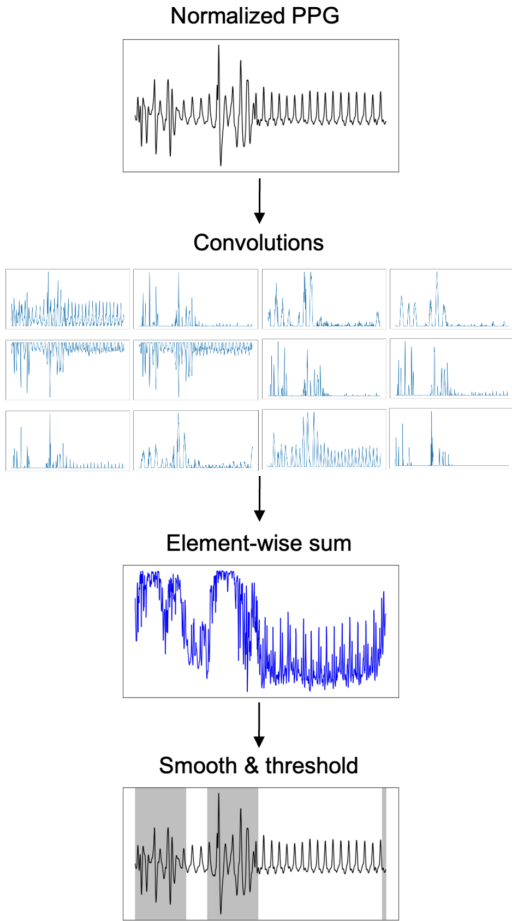


Figure 1: The processing pipeline for the PPG signal quality segmentation task. First, a PPG signal is normalized to a unit normal by subtracting the mean and dividing by the standard deviation. Next, a set of convolutions is applied. Note this figure shows *all of the signals after convolution*. The convolved signals are floored, weighted, and summed, and a sigmoid is applied. Finally, the output is smoothed and thresholded to segment the signal.

segmentation. This pipeline is shown in Figure 1.

More formally, our model consists of  $M$  kernels,  $M$  scalar biases, and  $M$  scalar weights. Given an input signal,  $\mathbf{x}$ , our learned kernels model ( $LK$ ) is defined as follows:

$$LK(\mathbf{x}) = \sigma \left( \sum_{m=0}^M \max(0, \mathbf{x} * \mathbf{k}_m + b_m) \cdot w_m \right)$$

where  $k_m$ ,  $b_m$ ,  $w_m$  are the  $m^{th}$  convolution kernel, bias, and signal weight respectively,  $*$  represents the convolution operation,  $\cdot$  is scalar-vector multiplication,  $+$  is the addition of a single scalar to all elements of a vector, and  $\sigma$  is the element-wise sigmoid function,  $(1 + e^{-\mathbf{x}})^{-1}$ . In essence, our model is equivalent to a linear combination of filtered signals generated by convolving the input with a learnable kernel, mapped to range  $(0, 1)$ . For the segmentation task, the output can be further post-processed via smoothing and thresholding to yield a segmentation map.

## 4.2 Data Pre-processing

Data was divided into 30-second chunks (1920 data points at 64 Hz) and normalized at the chunk level by subtracting the mean and dividing by the standard deviation. Normalization was performed at the chunk-level rather than the dataset-level to ensure that signal intensities remained relatively consistent regardless of the chunk being processed, improving generalization to distributions of PPG signals that may have different global parameters or greater inter-sample variability.

## 4.3 Training

To learn the kernels, we used stochastic gradient descent with Adam optimization [38] ( $\beta_1 = 0.9$ ,  $\beta_2 = 0.999$ ,  $\epsilon = 10^{-8}$ , weight decay =  $10^{-4}$ ), and a linear learning rate decay schedule (decaying from 0.01 to 0.002 learning rate on the final iteration), with a binary cross-entropy error objective function. Since our dataset is on the order of  $10^8$  bytes and our model

sizes are on the order of  $10^3$ - $10^5$  bytes, we can compute the gradient over the entire dataset in a single pass to obtain the true gradient (as opposed to an estimate via a mini-batch). For the largest model sizes, we use gradient accumulation due to memory constraints. Thus, we train for 512 iterations computing the gradient over the entire training set. We find that this yields empirically better performance than stochastic mini-batches. We also opt for such an extreme coverage of the training set (in terms of epoch count), as we find it empirically difficult to overfit the training data given our parameter count and iteration count, especially at smaller kernel numbers.

## 4.4 Parameter Reduction

We take several steps to further reduce parameter count to optimize the compute-to-performance ratio. These steps take place after the training procedure outlined in Figure 1 and are used for deployment.

### 4.4.1 Weight Absorption

We can reduce the parameter count of our model by absorbing the weighting factor into the kernels themselves, due to the “almost linear” property of the model. Let  $x$  be the input PPG signal, which is a vector of length 1920. Let  $k_m$ ,  $b_m$ ,  $w_m$  be the  $m^{th}$  convolution kernel, bias, and signal weight respectively. The kernels are vectors of length 192, 96, or 64 depending on the length class (long, moderate, or short), while the biases and weights are scalars. We have:

$$\begin{aligned} LK(\mathbf{x}) &= \sum_{m=0}^M \max(0, \mathbf{x} * \mathbf{k}_m + b_m) \cdot w_m \\ &= \sum_{m=0}^M \max(0, (\mathbf{x} * \mathbf{k}_m + b_m) \cdot |w_m|) \cdot \text{sgn}(w_m) \\ &= \sum_{m=0}^M \max(0, (\mathbf{x} * \mathbf{k}_m) \cdot |w_m| + b|w_m|) \cdot \text{sgn}(w_m) \\ &= \sum_{m=0}^M \max(0, [\mathbf{x} * (\mathbf{k}_m \cdot |w_m|)] + b|w_m|) \cdot \text{sgn}(w_m), \end{aligned}$$

$|\cdot|$  is an element-wise absolute value.

The quantity  $k \cdot |w_m|$  becomes the new kernel, and the quantity  $b|w_m|$  becomes the new bias. We reduce parameter count as we can now store the kernels themselves along with a corresponding binary value indicating whether they are positive or negative kernels. Furthermore, each kernel can be neatly categorized into “contributing to good signal quality” (positive kernels) or “contributing to poor signal quality” (negative kernels). This process is performed after learning the kernels, with the goal to reduce the memory footprint and number of scalar operations for deployed models.

### 4.4.2 Pruning

Driven by the observation that some learned kernels look quite similar, we hypothesized that we could prune similar kernels while maintaining good performance. To measure the similarity between kernels, we use the cosine similarity metric. Given two vectors  $v_1$  and  $v_2$ , the cosine similarity is defined as:

$$\text{similarity}(v_1, v_2) = \frac{v_1 \cdot v_2}{\|v_1\|_2 \|v_2\|_2}. \quad (1)$$

Cosine similarity measures the cosine of the angle between two vectors, resulting in a value between -1 and 1. A value of 1 indicates that the vectors are identical, while a value of -1 indicates that they are completely dissimilar.

Our kernel pruning method consists of the following steps:

1. For each convolutional layer, compute the cosine similarity between all pairs of kernels.
2. Sort the kernel pairs by their cosine similarity (in order of descending similarity), and select the top  $pa$  pairs to prune, where  $pa$  is a hyperparameter.
3. For each selected pair to prune, determine which of the two kernels to remove and which to keep based on their effective contribution to the signal (described below).

To determine which kernel to prune, we compute the “effective contribution” of the kernel as:

$$\text{eff}_j = w_j \cdot m_j, \quad \text{eff}_k = w_k \cdot m_k \quad (2)$$

where  $w_j$  and  $w_k$  are the weights of the two kernels in a pair and  $m_j$  and  $m_k$  are the mean absolute values of the kernels  $w_j$  and  $w_k$ , respectively. We keep the kernel with the higher effective weight and prune the other kernel.

When pruning a kernel, we need to update the weight and biases of the remaining kernel to correct for the removed kernel’s contribution. Without loss of generality, assume that  $\text{eff}_j > \text{eff}_k$ . We update the weight and bias of the remaining kernel  $i$  as follows:

$$w'_j = \frac{\text{eff}_j + \text{eff}_k}{m_j}, \quad b'_j = b_j + b_k. \quad (3)$$

where  $b_j$  and  $b_k$  are the biases for weight  $w_j$  and  $w_k$  respectively.

## 5 Experiments

The following experiments aim to compare our methodology to several common baselines, as well as a state-of-the-art multi-million parameter architecture based on U-Net. We show that our segmentation algorithm matches or exceeds the state-of-the-art in several benchmark PPG tasks.

### 5.1 Evaluation

To evaluate the performance of the baselines and learned kernels for artifact detection, we used the DICE score, defined as

$$DICE(A, B) = \frac{2|A \cap B|}{|A| + |B|}$$

where  $A$  and  $B$  are the binary segmentation maps of the predicted and ground truth, respectively, and  $|\cdot|$  denotes the cardinality of a set. We employed this score on a test set of PPG signals, with each 30-second chunk of PPG signal normalized via the method described earlier. We conducted 10-fold cross-validation using 10 different models trained from different starting seeds.

### 5.2 Baselines

We compare to the same baselines tested in Guo et al. [31]. Namely, a convolutional neural network sliding window approach, a template-matching approach, and a ResNet-34-based classifier with segmentation performed via GradCAM [32] or SHAP [33].

#### 5.2.1 Convolutional Sliding Window

Our first baseline is a 1D-convolutional network trained to classify 3-second windows of PPG signal as either “artifact” or “clean.” The network consists simply of 3 blocks of convolution-ReLU-BatchNorm-MaxPool. The 3 blocks consist of kernel sizes 10, 5, and 3, and the channel numbers are 64, 64, and 128. The model was trained from 5000 three-second windows that were randomly selected from the PPG-DaLiA training set. Training consisted of 200 epochs of minimizing cross-entropy loss with Adam. Testing was done by segmenting the 30-second PPG signal into 3 second chunks with the trained convolutional neural network classifier, and a sliding window with a step size of 1 second was used for testing. Since the trained convolutional network has an input size of 3-second chunks, each second of PPG signal receives 3 classification outputs. A 1-second chunk of PPG signal is classified as an artifact if *any* of the three classification outputs are classified as an artifact.

#### 5.2.2 Template-Matching

We follow the same approach as Guo et al. [31], which was inspired by Lim et al. [39]. Signals were first divided from the PPG-DaLiA training set into separate pulses via peak detection. 10 clean (artifact-free) pulses were then selected to serve as our standard templates for comparison with test pulses. Each pulse from the test data was compared to these 10 templates, using the dynamic time warping (DTW) distance metric to measure similarity. The smallest DTW distance (out of the 10 comparisons with the templates) was then identified. The range of the DTW distance function is  $[0, \infty)$ , but empirically we find that the DTW distances between our templates and the PPG signals fall mostly within the range

[0, 10]. We created a binary predicted label by labeling a segment as an artifact if the minimum DTW distance is at least 1. Other samples were given “non-artifact” predicted labels. The threshold of DTW was chosen by testing thresholds between 0 and 10 over the entire train set and choosing the threshold that produced the highest DICE score (which was 1). To summarize, if the minimum DTW distance  $\alpha$  exceeds our threshold, we classify the entire pulse (and all its timesteps) as an artifact.

### 5.2.3 GradCAM & SHAP

In this baseline experiment, the Resnet-34 architecture proposed by Dai et al (2016) was employed for 1D binary classification (identifying ‘clean’ or ‘artifact’). This architecture, traditionally used for image classification, was repurposed for time series analysis via GradCAM [32]. Considering the relatively small size of the training dataset, transfer learning was performed on a pre-trained Resnet34-1D PPG signal quality classifier, as described by Zhang et al (2021) [40]. This pre-trained model was originally trained on the UCSF PPG dataset according to Pereira et al (2019) [41]. The last two residual blocks, global average pooling, and the final dense layer were subsequently retrained by Guo et al. [31].

To train a classification model, ground truth labels were created such that any signal that contained artifact timesteps was labeled as an artifact, while all other signals were labeled as non-artifacts. After this labeling process, the training set consisted of 175 clean signals and 3261 artifact signals.

The model was trained using the Adam optimizer [38], using the binary cross-entropy loss. An initial learning rate of  $10^{-5}$  was set, which was scheduled to reduce to  $5 \times 10^{-6}$  after 10 epochs, and further decrease to  $1 \times 10^{-6}$  after 50 epochs. The maximum number of training epochs was capped at 100.

While the Resnet34-1D network is fundamentally a classifier, our goal is instead to obtain segmentation labels. Assuming that the model would focus on artifacts when tasked with predicting an artifact signal, we employed two post-hoc explanatory methods to generate segmentation masks: SHAP [33] and GradCAM [32].

SHAP is a unified measure of feature importance that assigns each feature an importance value for a particular prediction. It is based on game theory and computes Shapley values. The Shapley value of a feature represents the average marginal contribution of that feature across all possible feature subsets.

GradCAM utilizes the gradients of any target concept flowing into the final convolutional layer of a CNN to produce a coarse localization map highlighting the important regions in the image (or in this case, a time series) for predicting the concept. This is done by first computing the gradient of the output category with respect to feature maps of the last convolutional layer, then applying a global average pooling over the gradients to obtain weights for the feature maps. These weights are multiplied with the feature maps and summed over all maps to generate the final output. This output can be used as a heatmap, indicating which parts of the input were important in making the model’s prediction. GradCAM can be applied to any CNN-based network without requiring architectural changes or re-training.

For the SHAP values, the computed values were first smoothed with a Gaussian filter. A binary segmentation mask was then created by choosing the class with the higher SHAP value at each timestep.

### 5.3 Segade

Finally, we compare to the current state-of-the-art, Segmentation-based Artifact Detection (Segade) by Guo et al. [31]. Segade is a 1D segmentation network similar in architecture to UNet, with a few changes; notably, the convolutions are replaced with residual convolutions for better gradient propagation and the convolutions are one-dimensional as the data type is one-dimensional. We refer to [31] for a detailed discussion of the architecture.

## 6 Results

### 6.1 Test Set Performance

We find that our largest model significantly exceeds the performance (measured in DICE score)

of all baselines except the current state-of-the-art (Segade), for which it achieves >99% of its DICE-score on DaLiA and WESAD, **with less than 2% the parameter count of the state-of-the-art model**. Our largest model even manages to **significantly outperform all other baselines, including Segade, on the most challenging and least in-distribution dataset (TROIKA)**. Our medium model, at 0.4% of the parameter count of Segade, achieves at least 98% of Segade’s DICE score on all datasets and matches Segade’s performance on TROIKA. Lastly, our smallest model, at 0.06% of the parameter count of Segade, reaches 94% of the DICE score of Segade on DaLiA and WESAD, though struggles on TROIKA, reaching 86% of the DICE score of Segade. Detailed results and parameter counts are in Table 1.

## 6.2 Scaling Laws

In this section, we explore the scaling behavior of our approach by gradually increasing the number of kernels and evaluating the performance on the test set. Our main objective is to understand the relationship between the parameter count and test-set performance, which will help us identify the potential limits and robustness of our approach.

To investigate the scaling behavior, we first conduct a series of experiments with different numbers of kernels and measure the corresponding test-set performance using the DICE score. As anticipated, we observe an asymptotic relationship between the parameter count and the test-set performance, as shown in Figure 2.

Our analysis reveals that the test-set performance plateaus and remains roughly monotonically increasing as the parameter count increases, without exhibiting signs of overfitting. This finding suggests that our approach is robust even at extremely high parameter counts.

In summary, our exploration of scaling laws demonstrates an asymptotic relationship between parameter count and test-set performance, providing insights into the limits and robustness of our approach. The absence of overfitting at high parameter counts attests to the stability of our architecture.

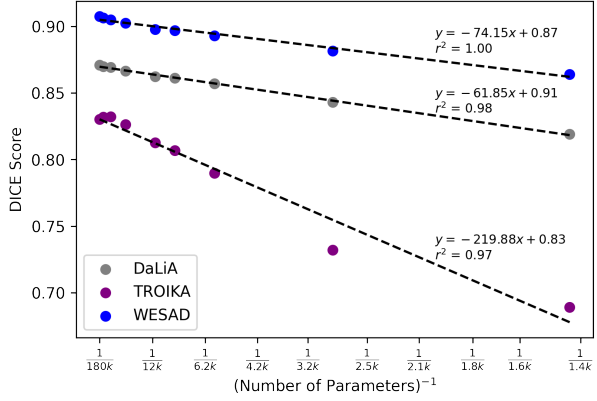


Figure 2: Exploration of scaling laws reveals an asymptotic relationship between inverse parameter count and DICE score.

We note that it is possible that a theoretical performance limit exists due to mislabelings in the test set; this is discussed further in the Discussion section.

## 6.3 Interpretability

A considerable benefit of our approach is clarity of the signal processing of the PPG, unlike in traditional deep neural networks. Since our model consists of a single layer of convolutions of varying kernel sizes, we can simply peer inside the model and determine how much each set of convolutions (and even each individual kernel) contributes to the overall classification signal.

To begin our exploration, we look to quantify the effect each kernel has on the output signal when presented with a perfect match to its signal. To compute the importance of the  $m^{th}$  kernel, we calculate the following expression:

$$\text{kernel importance}_m = \left( \sum_k \mathbf{k}_{m,k}^2 + b_m \right) \cdot w_m$$

where  $\sum_k \mathbf{k}_{m,k}^2$  is the sum of each squared component of the  $m^{th}$  kernel,  $b_m$  is the  $m^{th}$  kernel’s bias, and  $w_m$  is the  $m^{th}$  kernel’s weight. This, by definition, computes the value added to the final signal by

Model	PPG-DaLiA	WESAD	TROIKA	Params
Segade (SotA)	<b>0.8734 ± 0.0018</b>	<b>0.9114 ± 0.0033</b>	0.8050 ± 0.0116	<b>2.3M</b>
Sliding window	0.8068 ± 0.0014	0.8446 ± 0.0013	0.7247 ± 0.0050	<b>51K</b>
Template matching	0.6974 ± 0.0323	0.6954 ± 0.0309	0.6748 ± 0.0122	N/A
GradCAM	0.7129 ± 0.0010	0.7372 ± 0.0024	0.6989 ± 0.0034	<b>4M</b>
SHAP	0.6748 ± 0.0000	0.6634 ± 0.0000	0.6849 ± 0.0001	<b>4M</b>
<b>Learned Kernels (Small)</b>	0.8191 ± 0.0014	0.8639 ± 0.0015	0.6891 ± 0.0022	<b>1.4K</b>
<b>Learned Kernels (Medium)</b>	0.8610 ± 0.0005	0.8968 ± 0.0008	0.8067 ± 0.0075	<b>8.5K</b>
<b>Learned Kernels (Large)</b>	<i>0.8692 ± 0.0002</i>	<i>0.9050 ± 0.0002</i>	<b>0.8322 ± 0.0026</b>	<b>45.3K</b>

Table 1: Various baselines vs. our approach at varying parameter counts. Parameter counts above 1M are in **red** and parameters below 100K are in **blue**. Best results are bolded, and italicized results are at least 99% of the performance of the best result.

that kernel when the kernel perfectly overlaps with an exact template match. Furthermore, we also note that in the case of a normalized kernel and bias (i.e.  $\sum_k \mathbf{k}_{m,k}^2 + b_m = 1$ ), the kernel importance directly equals the weighting of that kernel. We run this kernel analysis across all 10 cross-validation models for the small, medium, and large model sizes.

We also compute and record the output values of each kernel group over the whole test dataset. Essentially, we perform the convolution and weighting operation for each set of kernels grouped by size (long, moderate, or short), along the entire test dataset, concatenating the output values to one array. We further segregate the output values depending on whether they were generated by PPG signals labeled as artifact or clean. In the framework of our model, this is equivalent to computing:

$$\sum_{\mathbf{k}, b, w \in \mathbf{K}, B, W} \max(0, \mathbf{x} * \mathbf{k} + b) \cdot w$$

where  $\mathbf{K}$ ,  $B$ , and  $W$  are the set of kernels, biases, and weights associated with the kernel group in question (i.e., the long, moderate, or short kernels).

We notice a clear pattern between kernel size and kernel importance. We find that for the medium and large models, the long kernels have significantly more positive ( $p < 10^{-13}$ ) mean importance than the short and moderate kernels, with significance computed via two-tailed independent samples t-tests. For the small model, the long and moderate kernels have a mean importance significantly more positive than the small

kernels ( $p < 10^{-6}$ ) (see Figure 3). These results indicate that long kernels generally learn to recognize poor-quality signal features, while medium and short kernels learn to recognize clean PPG features. We find this to be empirically true, with long kernels producing positive values most of the time, moderate kernels producing mostly negative or mixed positive/negative values (as seen in the medium-sized model), and short kernels producing mostly negative values (Figure 3). We demonstrate one such 30-second example of this in Figure 4. The agreement between our theoretical exploration of kernel importance and our empirical exploration of the values produced by various kernel groups over the test sets validates the interpretability of our model. These results are shown in Figure 3 by comparing the top and bottom rows.

Next, we note that because our smallest model consists of only 12 kernels, we can easily visually inspect each kernel. They are all shown in Figure 5. This is in stark contrast to compared to most deep-learning models, where the parameters are typically so numerous that it is intractable to manually inspect each parameter; here, *all* of them can be shown on one page. Furthermore, parameters in deep neural networks are typically uninterpretable, whereas our model represents a template-matching paradigm with a waveform.

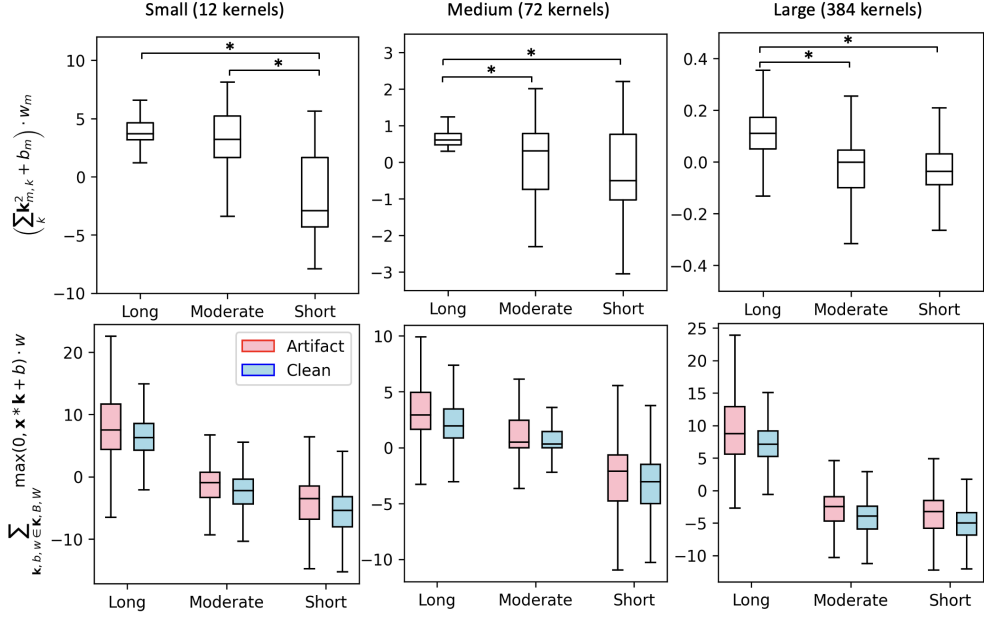


Figure 3: The computed ‘‘kernel importance’’ of each kind of kernel in each model size (top row) and the empirical output values of each kernel group observed over the clean and artifact parts of the dataset (bottom row). Significant differences in computed ‘‘kernel importances’’ are reflected in the empirical output values of those kernel groups over the test set. Notably, long kernels appear to play a large role in detecting artifacts, while short kernels appear to play a large role in recognizing clean PPG signals. The role of moderate kernels appears variable, but more often is involved in the recognition of clean PPG signals. (\*) denotes statistical significance at  $p < 10^{-6}$  via a two-tailed independent samples t-test with Bonferroni correction. All differences are significant between the empirical kernel output due to the extremely large sample size.

## 6.4 Pruning Experiments

We find that applying our pruning procedure on long kernels provides the greatest parameter reduction with the least performance trade-off. Pruning moderate and/or short kernels impacts performance more heavily and ultimately does not prune as many parameters as pruning long kernels, since each long kernel contains more parameters by definition. Ultimately, the choice of prune-to-performance ratio is up to the user and specific use case, though we provide an example pruning scheme in Table 2 which attempts to maintain performance around 96% of the mean original performance. Notably, as the model size increases, we are able to remove progressively more parameters with less of a decrease in perfor-

mance. We hypothesize this may be due to increased capacity of larger models and perhaps greater learned redundancy. Furthermore, because our model is a well-behaved ‘‘almost linear’’ system, model weights can be naïvely quantized with virtually no loss in performance. In fact, a simple cast from float32 to float16 yielded indistinguishable results. In contrast, the quantization process for a deep neural network is non-trivial, as error accumulates and propagates through the network.

## 6.5 Data Limitations

The extrapolated performance ceiling for our approach prompted an inspection of the test set. We computed the accuracy of our approach on each 30-

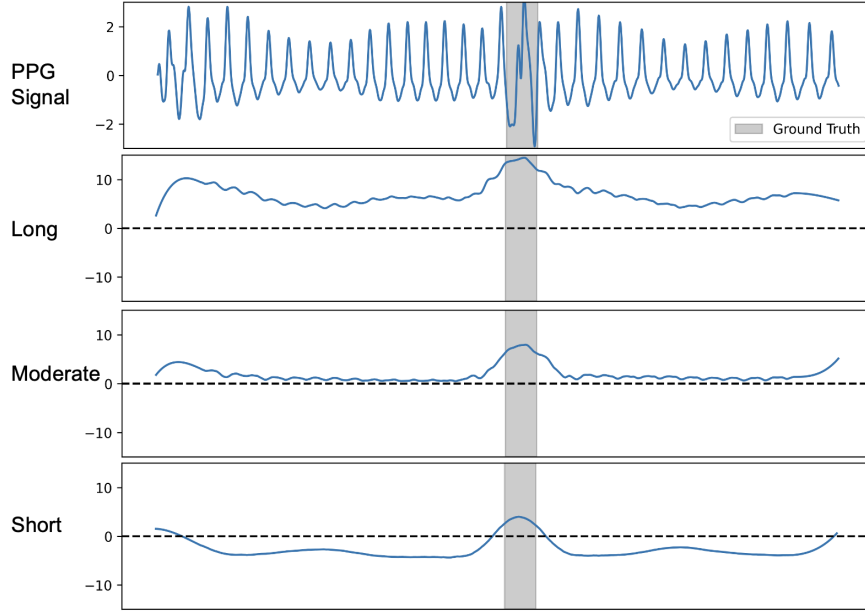


Figure 4: The contribution of each kernel group to the overall output signal. Noticeably, the “long” kernels have a positive signal even when convolved over clean segments, the “moderate” kernels have a signal close to zero when convolved over clean segments and a positive value over the artifact, and the “small” kernels have negative values except when convolved over the artifact.

second sample in the test set, then sorted the test set by accuracy. Upon inspection of the test set samples on which our approach performed the poorest, we find that the source of this disagreement corresponds to suboptimal labeling rather than inaccurate classification by our approach. In other words, our method was correct and the labels were wrong. Several such inaccuracies are shown in Figure 6. Many of these inaccuracies in labeling seem to stem from PPG signals that have abnormally low amplitude compared to other signals in the dataset. Although this is unusual, we do not consider it an artifact, since the PPG signal retains its structure and signal-to-noise ratio. Furthermore, a PPG signal could have diminished amplitude due to factors like light travel distance, the brightness of the source light, lessened perfusion of the appendage (e.g., if the appendage is cold), etc.

## 7 Discussion

We presented a novel, simple, and interpretable method for signal quality assessment using learned convolutions. Our approach achieved near state-of-the-art performance on three benchmark datasets with several orders of magnitude fewer parameters than deep learning methods and showing better generalization to out-of-distribution data, as evident by the markedly improved performance in the most out-of-distribution task, the TROIKA dataset. This method’s simplicity and interpretability allow for the inspection of the model’s inner workings, providing insights into the contribution of each kernel to the overall signal quality assessment. Furthermore, our method demonstrates extremely low compute and memory demands, setting it apart from deep-learning-based approaches. This enables high-quality signal assessment on low-power wearable devices.

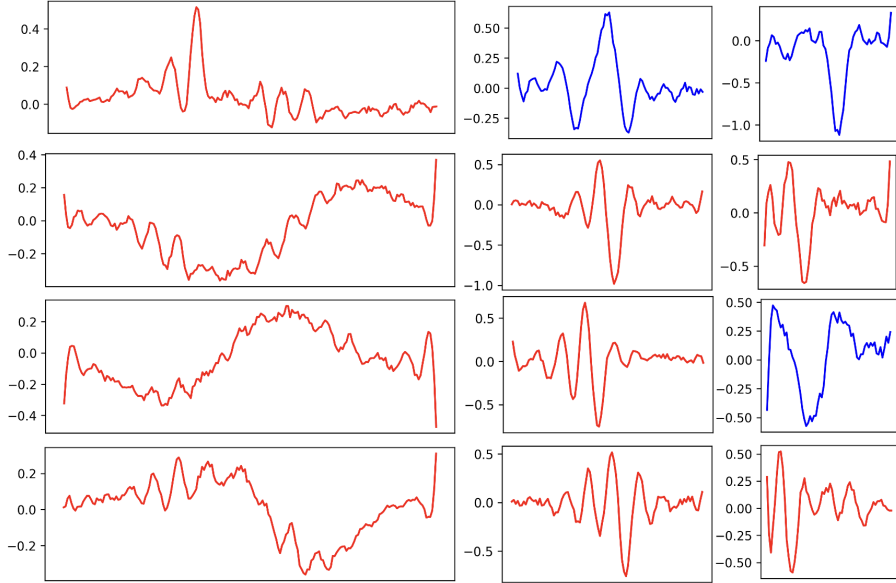


Figure 5: All 12 kernels of the small model. **Blue** kernels contribute primarily to the detection of “clean” signals and **red** kernels contribute primarily to the detection of artifacts.

Model	Removed	All	DaLiA	TROIKA	WESAD
Small	$13.6\% \pm 0.0\%$	$96.3\% \pm 4.7\%$	$95.2\% \pm 3.9\%$	$99.8\% \pm 0.5\%$	$94.5\% \pm 5.8\%$
Medium	$13.3\% \pm 1.6\%$	$96.8\% \pm 2.3\%$	$96.8\% \pm 1.7\%$	$96.7\% \pm 3.0\%$	$96.9\% \pm 1.9\%$
Large	$20.8\% \pm 1.4\%$	$95.7\% \pm 4.2\%$	$95.8\% \pm 3.9\%$	$96.0\% \pm 2.7\%$	$95.3\% \pm 5.4\%$

Table 2: Pruning experiments conducted on various model sizes across all 10 folds, listing the percentage of parameters removed, the percentage of the original mean performance across all datasets, and the percentage of original performance on DaLiA, TROIKA, and WESAD.

Our results demonstrated that our learned kernels can effectively capture relevant features for identifying good and poor-quality PPG signals. The scaling behavior of our approach showed a power-law relationship between parameter count and test-set performance. Our analysis of the kernel importance revealed that larger kernels primarily contribute to the identification of poor-quality signal features, while smaller and medium-sized kernels capture normal PPG features. Importantly, our work demonstrates that for some complex tasks, simple and interpretable models can perform just as well as deep neural networks and are even preferable.

Furthermore, we successfully applied parameter reduction techniques to improve the compute-to-performance ratio, keeping in mind the low-power limitations of wearable devices. We demonstrated that we can remove over 20% of parameters in large models and maintain above 97% of the original performance. We also demonstrated that, owing to the simplicity and near linearity of our model, we can naïvely quantize the model weights with no impact on performance. This is in stark contrast to deep neural networks, where the chaotic properties of the system can amplify and propagate error due to quantization, leading to performance degradation. Quantization is

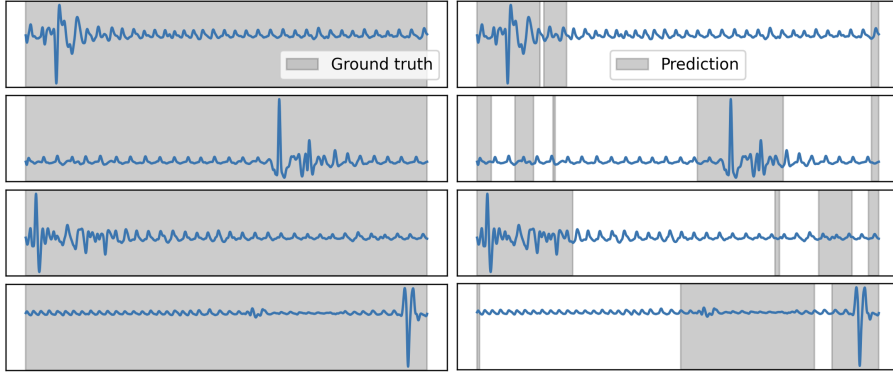


Figure 6: Ground truth labels for several 30-second PPG signal chunks are shown in comparison to their corresponding labels generated by the Learned Kernels. Notably, low-amplitude PPG signals that still retain their waveform are marked as artifacts in the ground truth. These segments are not marked as artifacts by the learned kernels, presumably because the signal retains a normal PPG waveform structure despite diminished amplitude, and because each 30-second PPG signal is normalized to its mean and standard deviation, thus eliminating amplitude changes locally.

also often a non-trivial process in deep neural networks as a result of dynamic range issues, again owing to the chaotic nature of neural networks. Our proposed method suffers from none of the aforementioned complexities.

All in all, our largest model can run in under 100 KB of memory when cast to float16 and can run in under 75 KB after weight pruning. Our smallest model runs using under 3 KB of memory cast to float16. Computing a raw (i.e., without post-process smoothing) signal score is extremely computationally efficient, with our largest model requiring on the order of 10 MFlops/second of signal processing. This memory-efficient and compute-efficient approach means that designers of low-power, wearable devices can now achieve state-of-the-art PPG signal quality assessment on extremely stringent compute budgets. This starkly contrasts with deep learning methods which are memory and compute-intensive. Additionally, implementation of our architecture is simple and straightforward to adapt to lower-level programming languages, whereas deep learning-based methods require the time-intensive reimplementation of complex deep learning operations into lower-level devices.

We also highlighted potential limitations in the datasets used for evaluation, as some labeling inaccuracies and discrepancies were observed in the test set samples with the poorest performance. This suggests that the practical maximum achievable performance for PPG artifact detection on these test sets may be limited by the quality of the available ground truth labels.

In conclusion, our method provides a robust, interpretable, and efficient approach for PPG signal quality assessment, making it competitive with deep learning approaches and suitable for deployment on low-power devices. Future work could focus on investigating the patterns observed in the kernel importances, further optimizing the model for improved performance, and addressing potential limitations in the training data to ensure more accurate and reliable results. Additionally, the application of our method to other physiological signals and tasks could be explored, as well as the integration of our approach with other wearable devices for real-time signal quality assessment.

## References

- [1] Daniel Ray, Tim Collins, Sandra I. Woolley, and Prasad V. S. Ponnappalli. A review of wearable multi-wavelength photoplethysmography. *IEEE Reviews in Biomedical Engineering*, 16:136–151, 2023.
- [2] Christoph Hoog Antink, Yen Mai, Mikko Peltokangas, Steffen Leonhardt, Niku Oksala, and Antti Vehkaoja. Accuracy of heart rate variability estimated with reflective wrist-PPG in elderly vascular patients. *Scientific Reports*, 11, 2021.
- [3] Xiaorong Ding, Wenjin Wang, Yifan Chen, Yumin Yang, Yan Zhao, and Deyuan Kong. Feasibility study of pulse width at half amplitude of camera ppg for contactless blood pressure estimation. In *2021 43rd Annual International Conference of the IEEE Engineering in Medicine & Biology Society (EMBC)*, pages 365–368, 2021.
- [4] David K. Spierer, Zohn Rosen, Leib L. Litman, and Kenji Fujii. Validation of photoplethysmography as a method to detect heart rate during rest and exercise. *Journal of Medical Engineering & Technology*, 39(5):264–271, 2015. PMID: 26112379.
- [5] P M Nabeel, J Jayaraj, and S Mohanasankar. Single-source ppg-based local pulse wave velocity measurement: a potential cuffless blood pressure estimation technique. *Physiological Measurement*, 38(12):2122, 2017.
- [6] Lena M. Nilsson. Respiration signals from photoplethysmography. *Anesthesia & Analgesia*, 117(4):859–865, 2013.
- [7] Denisse Castaneda, Aibhlin Esparza, Mohammad Ghamari, Cinna Soltanpur, and Homer Nazeran. A review on wearable photoplethysmography sensors and their potential future applications in health care. *International Journal of Biosensors & Bioelectronics*, 4(4), 2018.
- [8] Maik Pflugradt and Reinhold Orglmeister. Improved signal quality indication for photoplethysmographic signals incorporating motion artifact detection. In *2014 36th Annual International Conference of the IEEE Engineering in Medicine and Biology Society*, pages 1872–1875, 2014.
- [9] Alexandra-Maria Tăuțan, Alex Young, Eva Wentink, and Fokko Wieringa. Characterization and reduction of motion artifacts in photoplethysmographic signals from a wrist-worn device. In *2015 37th Annual International Conference of the IEEE Engineering in Medicine and Biology Society (EMBC)*, pages 6146–6149, 2015.
- [10] Mohamed Elgendi. Optimal signal quality index for photoplethysmogram signals. *Bioengineering*, 3(4), 2016.
- [11] Safa Cherif, Dominique Pastor, Quang-Thang Nguyen, and Erwan L’Her. Detection of artifacts on photoplethysmography signals using random distortion testing. In *2016 38th Annual International Conference of the IEEE Engineering in Medicine and Biology Society (EMBC)*, pages 6214–6217, 2016.
- [12] J. X. Sun, A. T. Reisner, and R. G. Mark. A signal abnormality index for arterial blood pressure waveforms. In *2006 Computers in Cardiology*, pages 13–16, 2006.
- [13] E. Lutin, D. Biswas, N. Simoes-Capela, C. Van Hoof, and N. Van Helleputte. Learning based quality indicator aiding heart rate estimation in wrist-worn ppg. In *2021 43rd Annual International Conference of the IEEE Engineering in Medicine & Biology Society (EMBC)*, pages 7063–7067, 2021.
- [14] Jianzhong Chen, Ke Sun, Yi Sun, and Xinxin Li. Signal quality assessment of ppg signals using stft time-frequency spectra and deep learning approaches. In *2021 43rd Annual International Conference of the IEEE Engineering in Medicine*

& Biology Society (EMBC), pages 1153–1156, 2021.

[15] Tom Edinburgh, Peter Smielewski, Marek Czosnyka, Manuel Cabeleira, Stephen J. Eglen, and Ari Ercole. Deepclean: Self-supervised artefact rejection for intensive care waveform data using deep generative learning. In Bart Depreitere, Geert Meyfroidt, and Fabian Güiza, editors, *Intracranial Pressure and Neuromonitoring XVII*, pages 235–241. Springer International Publishing, 2021.

[16] Filipa Esgalhado, Beatriz Fernandes, Valentina Vassilenko, Arnaldo Batista, and Sara Russo. The application of deep learning algorithms for ppg signal processing and classification. *Computers*, 10(12), 2021.

[17] Pankaj, Ashish Kumar, Rama Komaragiri, and Manjeet Kumar. A review on computation methods used in photoplethysmography signal analysis for heart rate estimation. *Archives of Computational Methods in Engineering*, 29(2):921–940, 2022.

[18] Shahid Ismail, Usman Akram, and Imran Siddiqi. Heart rate tracking in photoplethysmography signals affected by motion artifacts: a review. *EURASIP Journal on Advances in Signal Processing*, 2021(5), 2021.

[19] Syed Khairul Bashar, Dong Han, Shirin Hajeb-Mohammadalipour, Eric Ding, Cody Whitcomb, David D. McManus, and Ki H. Chon. Atrial fibrillation detection from wrist photoplethysmography signals using smartwatches. *Scientific Reports*, 9(1):15054, 2019.

[20] Levi B. Wood and H. Harry Asada. Noise cancellation model validation for reduced motion artifact wearable ppg sensors using mems accelerometers. In *2006 International Conference of the IEEE Engineering in Medicine and Biology Society*, pages 3525–3528, 2006.

[21] Swapnil Puranik and Aldo W. Morales. Heart rate estimation of ppg signals with simultaneous accelerometry using adaptive neural network filtering. *IEEE Transactions on Consumer Electronics*, 66(1):69–76, 2020.

[22] Shinsuke Hara, Takunori Shimazaki, Hiroyuki Okuhata, Hajime Nakamura, Takashi Kawabata, Kai Cai, and Tomohito Takubo. Parameter optimization of motion artifact canceling ppg-based heart rate sensor by means of cross validation. In *2017 11th International Symposium on Medical Information and Communication Technology (ISMICT)*, pages 73–76, 2017.

[23] Khawaja Taimoor Tanweer, Syed Rafay Hasan, and Awais Mehmood Kamboh. Motion artifact reduction from ppg signals during intense exercise using filtered X-LMS. In *2017 IEEE International Symposium on Circuits and Systems (ISCAS)*, pages 1–4, 2017.

[24] Chih-Chin Wu, I-Wei Chen, and Wai-Chi Fang. An implementation of motion artifacts elimination for ppg signal processing based on recursive least squares adaptive filter. In *2017 IEEE Biomedical Circuits and Systems Conference (BioCAS)*, pages 1–4, 2017.

[25] Shao Hanyu and Chen Xiaohui. Motion artifact detection and reduction in ppg signals based on statistics analysis. In *2017 29th Chinese Control And Decision Conference (CCDC)*, pages 3114–3119, 2017.

[26] Nandakumar Selvaraj, Yitzhak Mendelson, Kirk H. Shelley, David G. Silverman, and Ki H. Chon. Statistical approach for the detection of motion/noise artifacts in photoplethysmogram. In *2011 Annual International Conference of the IEEE Engineering in Medicine and Biology Society*, pages 4972–4975, 2011.

[27] Wei-Jheng Lin and Hsi-Pin Ma. A physiological information extraction method based on wearable ppg sensors with motion artifact removal. In *2016 IEEE International Conference on Communications (ICC)*, pages 1–6, 2016.

[28] Tasbiraha Athaya and Sunwoong Choi. An efficient fingertip photoplethysmographic signal artifact detection method: A machine learning approach. *Journal of Sensors*, 2021, 2021.

[29] Choon-Hian Goh, Li Kuo Tan, Nigel H. Lovell, Siew-Cheok Ng, Maw Pin Tan, and Einly Lim. Robust ppg motion artifact detection using a 1-d convolution neural network. *Computer Methods and Programs in Biomedicine*, 196:105596, 2020.

[30] Xin Liu, Qihan Hu, Han Yuan, and Cuiwei Yang. Motion artifact detection in ppg signals based on gramian angular field and 2-D-CNN. In *2020 13th International Congress on Image and Signal Processing, BioMedical Engineering and Informatics (CISP-BMEI)*, pages 743–747, 2020.

[31] Zhicheng Guo, Cheng Ding, Xiao Hu, and Cynthia Rudin. A supervised machine learning semantic segmentation approach for detecting artifacts in plethysmography signals from wearables. *Physiological Measurement*, 42(12):125003, Dec 2021.

[32] Ramprasaath R. Selvaraju, Michael Cogswell, Abhishek Das, Ramakrishna Vedantam, Devi Parikh, and Dhruv Batra. Grad-cam: Visual explanations from deep networks via gradient-based localization. In *2017 IEEE International Conference on Computer Vision (ICCV)*, pages 618–626, 2017.

[33] Hugh Chen, Scott M. Lundberg, and Su-In Lee. Explaining a series of models by propagating shapley values. *Nature Communications*, 13(1):4512, 2022.

[34] David Pollreisz and Nima TaheriNejad. Detection and removal of motion artifacts in ppg signals. *Mobile Networks and Applications*, 27(2):728–738, 2022.

[35] Attila Reiss, Ina Indlekofer, Philip Schmidt, and Kristof Van Laerhoven. Deep ppg: Large-scale heart rate estimation with convolutional neural networks. *Sensors*, 19(14), 2019.

[36] Philip Schmidt, Attila Reiss, Robert Duerichen, Claus Marberger, and Kristof Van Laerhoven. Introducing wesad, a multimodal dataset for wearable stress and affect detection. In *Proceedings of the 20th ACM International Conference on Multimodal Interaction, ICMI '18*, page 400–408, New York, NY, USA, 2018. Association for Computing Machinery.

[37] Zhilin Zhang, Zhouyue Pi, and Benyuan Liu. Troika: A general framework for heart rate monitoring using wrist-type photoplethysmographic signals during intensive physical exercise. *IEEE Transactions on Biomedical Engineering*, 62(2):522–531, 2015.

[38] Diederik P. Kingma and Jimmy Ba. Adam: A method for stochastic optimization. In *Proceedings of the 3rd International Conference on Learning Representations*, 2015.

[39] Pooi Khoon Lim, Siew-Cheok Ng, Nigel H Lovell, Yong Poh Yu, Maw Pin Tan, Devin McCombie, Einly Lim, and Stephen J Redmond. Adaptive template matching of photoplethysmogram pulses to detect motion artefact. *Physiological Measurement*, 39(10):105005, oct 2018.

[40] Oliver Zhang, Cheng Ding, Tania Pereira, Ran Xiao, Kais Gadhouni, Karl Meisel, Randall J. Lee, Yiran Chen, and Xiao Hu. Explainability metrics of deep convolutional networks for photoplethysmography quality assessment. *IEEE Access*, 9:29736–29745, 2021.

[41] Tania Pereira, Nate Tran, Kais Gadhouni, Michele M. Pelter, Duc H. Do, Randall J. Lee, Rene Colorado, Karl Meisel, and Xiao Hu. Photoplethysmography based atrial fibrillation detection: a review. *npj Digital Medicine*, 3(3), 2020.